Partial selenium surface modulation of metal organic framework assisted cobalt sulfide hollow spheres for high performance bifunctional oxygen electrocatalysis and rechargeable zinc-air batteries

Alagan Muthurasu [a], Prabhakaran Sampath [a], Tae Hoon Ko [a], Prakash Chandra Lohani [a], Ishwor Pathak [a], Debendra Acharya [a], Kisan Chhetri [a], Do Hwan Kim [c,*], Hak Yong Kim [a,b,**]

[a] *Department of Nano Convergence Engineering, Jeonbuk National University, Jeonju 561-756, the Republic of Korea*
[b] *Department of Organic Materials and Fiber Engineering, Jeonbuk National University, Jeonju 561-756, the Republic of Korea*
[c] *Division of Science Education, Graduate School of the Department of Energy Storage/Conversion Engineering, Jeonbuk National University, Jeonju, Jeonbuk 54896, the Republic of Korea*

ARTICLE INFO

ABSTRACT

There is still a significant technological barrier in the development of high-performance electrocatalysts with synergistic unreliable functions and morphological integrity that improves reversible electrochemical activity, electrical conductivity, and mass transport properties. Metal-organic compound networks are envisioned as a defect-rich porous framework that provides mesoporous hollow carbon nanostructures composed primarily of an in situ-grown N-doped graphitic carbon matrix and embedded selenium-doped CoS_2 hollow spheres as efficient, highly reactive, and long-lasting chemical energy conversion functions of the system. This method enables hitherto inaccessible synthesis approaches to produce a highly porous conductive network at the microscopic level while exposing rich unsaturated reactive sites at the atomic level without losing electrical or structural integrity. Because of their inherent increased electrochemical surface area, and electron transfer, the porous framework, doping motifs, and tailored structural defects provide outstanding bifunctional oxygen electrocatalysts for both oxygen reduction reaction (ORR) and oxygen evolution reactions (OER). Moreover, using this selenium-doped MOF CoS_2 hollow spheres electrode as an air-cathode, a rechargeable zinc-air battery with excellent discharge-charge performance and mechanical stability is successfully constructed. This study provides a feasible and universal technique for constructing diverse functional interconnected metal-organic coordinated compounds that may be employed for a wide variety of energy storage, conversion (e.g., fuel cells and metal-air batteries), and environmental applications.

1. Introduction

In order to address the difficulties of natural resource depletion, climate change, and environmental damage, it is critical to developing innovative, sustainable, high-performance energy storage and conversion technologies rather than depending on current energy sources and fuel-based energy technologies [1,2]. Zn–air batteries (ZnABs) are a feasible device for fulfilling global energy demands owing to their high theoretical energy density (1086 Wh kg^{-1}) and implicit reliability resulting from the use of an aqueous electrolyte, and other benefits like low price, wide availability, and environmental friendliness [3]. As a result, there has been a lot of interest in developing high-activity rechargeable zinc-air batteries all around the world. The two primary processes of ZnABs that facilitate the simultaneous transfer of chemical and electrochemical activity are the oxygen evolution reaction (OER) during charging and the oxygen reduction reaction (ORR) when discharging [4,5]. The ORR and OER are well anticipated to be multi-electron reactions that take place at multi-phase interfaces and so have slow kinetics, leading to high voltage differences, poor energy efficiency, and low cycle stability. Subsequently, the inferior cathode kinetics in terms of ORR and OER is perceived as an impediment to the commercialization of rechargeable zinc-air batteries [6].

To tackle the kinetic challenge of the air cathode, where bifunctional electrocatalytic processes for ORR and OER are expected to facilitate rechargeable zinc–air batteries, the development of a high-performance ORR/OER bifunctional electrocatalyst is a viable option.[7,8] In particular, the potential gap (E) between both the half-wave potential ($E_{1/2}$) for ORR and the potential necessary to achieve a current density of 10 mA cm^{-2} for OER is frequently utilized to evaluate the ORR/OER bifunctional electrocatalytic capabilities [9]. Till date, Pt/C has been well established as a vastly more efficient ORR catalyst, whereas IrO$_2$ has shown promising properties in OER. Nonetheless, the ubiquitous usage of Pt/C and IrO$_2$ is hampered by their significant expense, shortage, and poor cyclic stability [10,11]. In this circumstance, the availability of more efficient bifunctional catalysts at a low price and with excellent durability has emerged as the major challenge for improving air-electrode electrochemical performance and, eventually, ZnAB operating efficiency. Thus, the development of a catalyst made of earth-abundant, ecologically friendly, and cost-effective elements is crucial [12,13]. Transition metal chalcogenides (TMCs) MX$_2$ (M = Co, Ni, Mo, W, etc.; X = S, Se, etc.) have been extensively utilized in electrochemical devices over the last two decades [14,15]. Among the various TMCs, cobalt pyrite (CoS$_2$, CoSe$_2$), a pyrite-type transition metal dichalcogenide, has previously been found beneficial in the field of electrochemistry due to its unique properties [16]. Based on theoretical and experimental research, these pyrite-type transition-metal dichalcogenides have emerged as low-cost materials with excellent water-splitting activity. It is commonly known that the following procedure can boost their catalytic performance [17–19]. To begin, the features of the heterojunction interface can be adjusted by building a heterojunction or composite structure to increase electronic transmission. Additionally, surface treatment (doping) of structural defects is an important technique for improving electrochemical properties [20–24]. The synthesis of heterojunction materials with hollow structures is crucial for the fabrication of effective and stable electrocatalysts for the reasons described above. Prior research has found that modest doping may significantly boost electrochemical catalytic activity. In this aspect, the properties of selenide products outperform those of other materials (for example, sulfur), which might be attributed to the reasons given: The Se atom possesses higher electronegativity than the S atom and can thus replace it in a high-temperature reaction process [25,26] . In contrast to S, Se forms a new bond with another element, causing the interlayer distance to change, enabling electron transport at the interface region and, eventually, increasing electrocatalytic activity [26]. As a result, selenium doping is an essential strategy for increasing the performance of electrochemical catalytic systems.

Particularly inspiring, Metal-organic frameworks (MOFs) have evolved as a potentially promising platform for the development of novel materials for sustainable energy conversion and storage systems. MOFs offer numerous important structural and compositional advantages over conventional materials due to perfectly ordered and tunable metal nodes and organic linkers. Because of the highly ordered configuration of metal nodes and organic ligands, consistent and numerous active sites with well-defined morphologies are synthesized [27]. In terms of structural considerations, MOFs, which have a variable nanostructure, high porosity, and a large specific surface area, has piqued the interest of scientists from a wide range of disciplines [28]. Zeolitic imidazolate frameworks (ZIFs) have been demonstrated to be suitable scaffolds for the development of hollow structures comprising metal-/metal oxide/metal sulfide [29]. By depositing ZIF on spherical templates and selectively removing the core-templates, hollow structures based on ZIF have been constructed [30,31]. It has also been proposed that solid ZIF can be transformed into a hollow structure using solvothermal treatment or etching techniques to investigate simple and cost-effective procedures [32]. Nevertheless, completely eliminating the templates or ZIF cores may destroy the typical ordered porosity structure and cause drawbacks such as channel blockage in the shell, needing careful control to minimize poor durability and rate capability caused by over-etching

[33]. Several studies have found that employing Co and ZIF as carbon sources, reductive annealing may convert solid ZIF into a hollow structure covered with self-grown Co, Co$_x$S, and CNT [34,35]. In these kinds of systems, the bulk of the sulfur aggregates on the surface of the hollow during cycling, while the inner cavity of the hollow continues to be a challenge.

In this work, we provide a simple and robust method for fabricating mesoporous and polar hollow-structured surfaces using ZIF chemistry. We synthesized and studied a hollow structure in which hollow primary spheres form a 500–600 nm framework without the need for a surfactant or template. As synthesized ZIF-67 hollow spheres were sulfurated/selenylated to produce Se-doped MOF CoS$_2$ hollow spheres. Doping alters the electrical structure of the material, allowing for faster electron transport during the catalytic performance. Simultaneously, the distinctive mesoporous hollow structure of Se-doped MOF CoS$_2$ hollow spheres allows total access to catalytically active sites in electrolytes. As a result, the developed Se-doped MOF CoS$_2$ hollow structure demonstrated superior bifunctional catalytic activity toward the ORR and OER in alkaline media, with increased water electrolytic current under low overpotential, a modest Tafel slope, and remarkable long-term stabilities. A rechargeable Zn-air battery is developed using Se-doped MOF CoS$_2$ hollow spheres as the air-cathode, resulting in exceptional discharge-charge behavior due to the Se doping (active sites) and mesoporous hollow structure boosting the charge/mass transfer channel (Scheme 1).

2. Experimental section

2.1. Chemicals

Cobalt (II) sulfate heptahydrate (CoSO$_4$·7 H$_2$O, 99%), and 2-Methylimidazole (99%), absolute were purchased from Sigma Aldrich. Sulfur powder (99.999%) was purchased from Alfa Aesar. Selenium powder (98%) was purchased from Samchun Chemical Reagent Co. Ltd. Ltd. Methanol was obtained from DUKSAN, Korea. All chemicals were used as received without further purification.

2.2. Synthesis of ZIF-67 hollow spheres

The hollow-structured ZIF-67 spheres was developed using cobalt sulfate and 2-methyl imidazole. Initially, cobalt sulfate heptahydrate solution (20 mmol of CoSO$_4$ 7 H$_2$O) and 2-methylimidazole solution (160 mmol of 2-MIM) were dissolved in separate 400 mL 100% methanol solutions. Then, the clear 2-Methylimidazole solution was mixed with the cobalt sulfate solution to make a uniform solution. Purple-colored precipitates of hollow ZIF-67 spheres were obtained after multiple washes with methanol and water. After washing, the purple-colored product was dried overnight at 60 °C.

2.3. Synthesis of MOF CoS$_2$ hollow spheres

The MOF CoS$_2$ hollow spheres was synthesized using the normal melt diffusion method. Typically, synthesized hollow ZIF-67 spheres were mixed with S powder at a weight ratio of 2:1 for 15 min. After that, the mixture was placed in an inert atmosphere reactor and heated at 500 °C for 3 h at a heating rate of 2 °C min^{-1} to obtain MOF CoS$_2$ hollow spheres.

2.4. Synthesis of Se doped MOF CoS$_2$ hollow spheres

The entire procedure was substantially similar to the previous technique for synthesizing MOF CoS$_2$ hollow spheres, except for changing the S powder (0.1 g) with a mixture of S powder (0.08 g) and Se powder (0.02 g). The mixture was then placed in an inert atmosphere reactor and heated at 500 °C for 3 h at a heating rate of 2 °C min^{-1} to obtain Se-doped MOF CoS$_2$ hollow spheres.
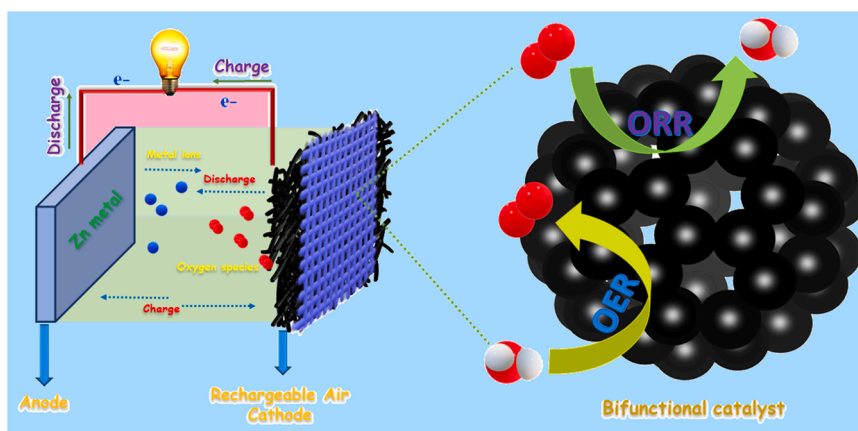
Scheme 1. Schematic illustration of the synthesized bifunctional Se-doped MOF CoS_2 hollow spheres electrocatalyst for rechargeable Zn-air batteries.

2.5. Electrochemical measurements

Electrochemical experiments tests for ORR and OER were carried out using a standard three-electrode setup outfitted with a computer-controlled workstation (VersaSTAT 4, USA) at room temperature. The electrochemical experiments were all performed in a 1.0 M KOH solution. As the counter and reference electrodes, a Pt foil and a conventional Ag/AgCl electrode with saturated KCl filling solution were used. The working electrode is a carbon cloth impregnated with a catalyst ink solution. The catalyst ink was made by the ultrasonic-assisted combination of 5 mg of synthesized material, ethanol (200 μL), deionized water (250 μL), and Nafion (50 μL) for 30 min to achieve a homogeneous mixture. The as-prepared homogenous catalyst ink solution (50 μL) was then drop-casted on clean carbon cloth (1.0 cm × 1.0 cm) and allowed to dry at 60 °C in an electrical oven which was then utilized as the working electrode in the electrochemical experiments. The Se-doped MOF CoS_2 hollow spheres catalyst loading was estimated to be 0.5 mg cm^{-2}. Additionally, the Pt/C and IrO_2 catalysts, which are considered one the most efficient noble-metal catalysts, were used as the catalytic benchmark for ORR and OER performance. Linear sweep voltammograms (LSV) were recorded at a sweep rate of 5 mV s^{-1}, and an electrochemical cyclic stability and long-term stability test for cyclic voltammetry (CV) cycle at a scan rate of 50 mV s^{-1} and chronoamperometry (CA) at constant overpotential. Electrochemical impedance spectroscopy (EIS) experiments were performed at frequencies ranging from 0.01 Hz to 100 kHz. Moreover, all electrochemical results were normalized to the reversible hydrogen electrode (RHE) using the Nernst equation and compensated for iR compensation.

2.5.1. For ORR measurements

The VersaSTAT 4 electrochemical workstation equipped with a rotating disk electrode (RDE) was utilized for ORR studies using a conventional three-electrode configuration at ambient temperature. Pt/C, Ag/AgCl, and RDE (5 mm: 0.19625 cm^2) were employed as the counter, reference, and working electrodes, respectively. For each electrochemical experiment, the reference electrode was calibrated against RHE. To make a homogenous ink solution, 2.5 mg of catalyst and 10 μL of 5% Nafion solution were dispersed in 1 mL of isopropyl alcohol and DI water (1:1) solution and sonicated for 60 min. Nearly 30 μL of catalyst ink was drop-coated onto a rotating disk electrode (RDE: diameter of 5.0 mm). A commercially available 20 wt% Pt/C catalyst ink was prepared similarly and coated on the RDE electrode for the comparison investigation. Cyclic voltammetry (CV), and liner-sweep voltammetry (LSV) were performed in a N_2 or O_2-saturated 0.1 M KOH electrolyte. LSV was also measured with different RDE rotation rates ranging from 100 to 2500 rpm. Before each ORR test, the electrolyte was bubbled with O_2 for 30 min. O_2 flow was maintained

throughout the measurements to ensure O_2 saturation. The methanol tolerance study was carried out using chronoamperometry and 0.5 M methanol in O_2 saturated 0.1 M KOH with a constant rotation of 1600 rpm. The chronoamperometric technique was used for the long-term test, which sustained 40 h at a constant potential of 1600 rpm in O_2 saturated 0.1 M KOH. The cycle durability was tested at 50 mV s^{-1} with 0.1 M KOH and O_2-saturated.

2.6. Aqueous Zn-air batteries

The liquid Zn-air battery was investigated in a homemade electrochemical cell. The aqueous Zn-air battery was built utilizing a commercial Zn foil (zinc foil (0.25 mm thick, Alfa Aesar, USA) anode and synthesized Se doped CoS_2 spheres air cathode and 6.0 M KOH as electrolyte. In comparison, a similar ZnAB was constructed by using the same protocols and a 1:1 mixture of IrO_2 and Pt/C as catalysts. Open circuit voltage, polarization curves, and galvanostatic discharge curves were examined using the electrochemical workstation.

2.7. Characterization

X-ray diffraction (XRD, Rigaku Co., Japan) using Cu-K source radiation ($\chi = 1.54178$) at a scan rate of 2° min^{-1} was used to analyze the phase purity and crystal structure of the catalyst. The surface morphology of the as-synthesized catalyst was captured using scanning electron microscopy (SEM) on a Hitachi, S7400 with an accelerated voltage of 15 kV field emission scanning electron microscope. The microstructure of the catalyst was investigated using a high-resolution transmission electron microscope (JEOL JEM 2010 with an operating voltage of 200 kV) and the related energy dispersive X-ray (EDX) spectra. Thermo Scientific KA1066 Spectrometer with a monochromatic Al K source was used to perform X-ray photoelectron spectroscopy (XPS) studies. The Brunauer–Emmett–Teller (BET) specific surface area and pore size distribution were performed using N_2 physisorption (Micromeritics, 3Flex 5.01).

2.8. Density functional theory (DFT) methods

Based on the data obtained by XRD results, the electrocatalyst was further thoroughly examined by computational analysis of DFT calculations using the Vienna Ab initio Simulation Package (VASP) [36,37]. The Perdew–Burke–Ernzerhof (PBE) exchange-correlation functional was applied along with Grimme's DFT-D3 functional with a semi-empirical GGA-type theory [38]. The projector augmented wave method (PAW), as implemented in VASP was used for ion-electron interactions [39]. To avoid the interaction between slabs, a vacuum layer of 15 Å was applied in the Z direction. Plane-wave basis set 400 eV was

fixed as cut-off energy. The structures were relaxed totally until the Hellman-Feynman forces were lower than 0.02 eV/Å. For energy and DOS calculations, the Γ-point-centered k-point meshes of $4 \times 4 \times 1$ and $8 \times 8 \times 1$ was used for Brillouin zone integrations [37]. Supporting information is provided for a more detailed discussion.

3. Results and discussion

3.1. Synthesis, morphological and structural characterizations of Se-doped MOF CoS$_2$ hollow spheres

Fig. 1 shows a schematic representation of the experimental procedure for preparing the mesoporous hollow structure of Se-doped MOF CoS$_2$ hollow spheres. Selenium-doped cobalt sulfide (Se doped MOF CoS$_2$), as well as MOF CoS$_2$ hollow spheres, MOF CoSe hollow spheres, and MOF Co hollow spheres samples for comparison, are synthesized in a two-step procedure that involves a solution technique and a sulfuration-selenization reaction. The entire preparation procedure is described in the experimental section. In stage one, the spherical hollow ZIF-67 is synthesized as a precursor using SO$_4^{2-}$ anions and methanol in a room-temperature solution approach. In stage two, hollow structures of Se-doped MOF CoS$_2$ spheres, MOF CoS$_2$ hollow spheres, and MOF CoSe hollow spheres are synthesized after the precursor interacts with pure S, a combination of S and Se, and pure Se, respectively. The mesoporous hollow structure of Se-doped CoS$_2$ hollow spheres was developed for use with ZIF-67 in this study; the formation process is described below. To begin, the unique mixture of methanol (CH$_3$OH) and SO$_4^{2-}$ ions allows the synthesis of ZIF-67 hollow spheres without the use of a template. According to electrostatic theory, a solvent with a low dielectric constant reduces the radius of the nuclei [40]. As a result, the low dielectric constant of CH$_3$OH (32.7) reduces the radius of the nuclei, causing the solution to become more thoroughly saturated and increasing the nucleation rate when these variables promote homogenous nucleation and spherical particle formation [41]. Furthermore, SO$_4^{2-}$ is more reactive to metal cations than other anions such as NO$_3^-$ or Cl$^-$ [42]. The strongly coordinated SO$_4^{2-}$ in solution might promote substantial disassembly of Co^{2+} and 2-MIM from ZIF-67, facilitating the inside-out Ostwald ripening mechanism in which the hollow structure appears as a result of dissolution-recrystallization involving mass transfer from the core region with smaller crystallites to the shell region with larger crystallites [43,44]. Field emission scanning electron microscopy (FESEM) images of synthesized MOF Co hollow spheres at various magnifications are shown in Fig. S1. The hollow nature of the synthesized MOF Co hollow spheres was clearly demonstrated, and the average diameter of the hollow spheres was about 500–600 nm. The energy dispersive X-ray (EDX) spectrum of the annealing product is shown in Fig. S1, where the Co/C/N ratio is about 1:1.28:0.5, indicating the presence of hollow MOF Co spheres. Elemental mapping is a tool used to investigate the distribution of various elements in MOF Co hollow spheres. As illustrated in Fig. S1, the result contains a homogeneous distribution of Co, C, and N elements. Similarly, following sulfuration and selenization, FESEM images at various magnifications demonstrate

the hollow nature of materials and their mesoporous surface (Fig. 2A-C). Throughout all steps, the average diameter of the hollow spheres remained relatively consistent. The precursor MOF Co hollow spheres, Se-doped MOF CoS$_2$ hollow spheres, are easily generated by random selenium doping during the high-temperature sulfuration/selenization technique, which can be interstitial doping or in situ replacement. Based on the molecular dynamics concept, the Co^{2+} in MOF induces the formation of CoS$_2$ with S powder [45]. Furthermore, Selenium also has a role in the response. Selenium atoms easily replace sulfur atoms or occur as interstitial doping at high temperatures [46], resulting in the formation of Se-doped MOF CoS$_2$ hollow spheres. The increased number of active sites generated by selenium doping contributes significantly to the eventual electrochemical performance improvement. Energy-dispersive spectroscopy (EDX) reveals the existence of cobalt (Co), Sulfur (S), selenium (Se), carbon (C), nitrogen (N), and oxygen (O), as illustrated in Fig. 2D. Fig. 2E-L depicts the elemental mapping for the Se-doped MOF CoS$_2$ hollow spheres sample. The elemental mapping representations of Co, S, Se, C, N, and O are shown in a variety of colors. The mapping results indicated that the constituent components Co, S, Se, C, N, and O were uniformly distributed across the whole Se-doped MOF CoS$_2$ hollow spheres sample. Additionally, the MOF Co hollow spheres precursor may result in the formation of MOF CoS$_2$ hollow spheres (Fig. S2) and MOF CoSe hollow spheres (Fig. S3). FESEM images of CoS$_2$ and CoSe show that the diameter of the spherical hollow structure did not change during the reaction process, and the corresponding EDX of MOF CoS$_2$ hollow spheres and MOF CoSe hollow spheres, as well as the respective elemental mapping, show a homogeneous distribution of all elements throughout the samples.

The precise structure and morphology of Se-doped MOF CoS$_2$ hollow spheres was confirmed using a transmission electron microscope (TEM). The TEM images with low and high magnification images are presented in Fig. 3A, B, which reveals that the Se-doped MOF CoS$_2$ spheres exhibit a hollow structure with a mesoporous surface and a particle diameter in the 500–600 nm range. Fig. 3C shows high-resolution TEM (HRTEM) images of the Se doped MOF CoS$_2$ hollow spheres lattice fringes, where the lattice spacings of Se doped MOF CoS$_2$ hollow spheres are 0.240 nm and 0.276 nm, respectively, well-matched with the crystal structures of (2 1 0) and (2 0 0) planes of CoS$_2$ [47]. Moreover, HRTEM shows that CoSe has no interfacial spacing, meaning that Se has been effectively doped into CoS$_2$, confirming the presence of CoS$_2$ after sulfidation and selenization. The SAED patterns image of the Se-doped MOF CoS$_2$ hollow spheres (inset Fig. 3C) showed fewer bright spots, indicating polycrystallinity or poor crystallinity. This might be because of the existence of two types of components. Furthermore, the existence of Co, S, Se, C, N, and O in Se-doped MOF CoS$_2$ hollow spheres was verified by the HR-EDX spectrum (Fig. 3L). The HR-EDX elemental mapping of the Se-doped MOF CoS$_2$ hollow spheres is shown in Fig. 3D-K. The Co, S, Se, C, N, and O constituents are distributed uniformly throughout the product.

As depicted in Fig. 4A, the X-ray diffraction (XRD) technique is utilized to examine the structural information of diverse materials. Fig. 4A (a) shows the XRD patterns of Se doped MOF CoS$_2$ hollow spheres
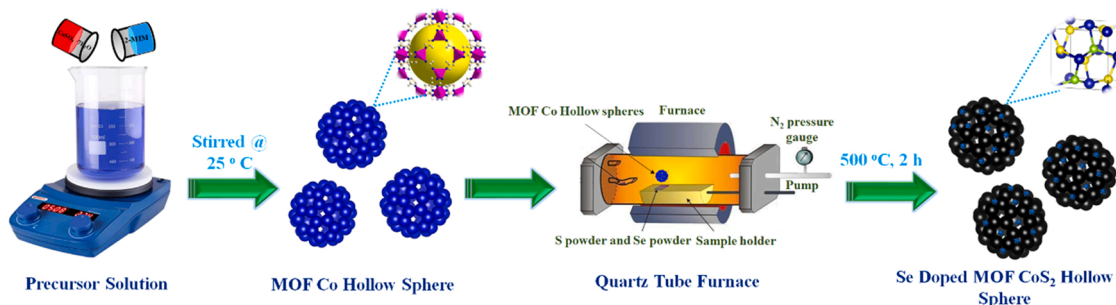

Fig. 1. Synthetic procedure for the preparation of Se-doped MOF CoS$_2$ hollow spheres.
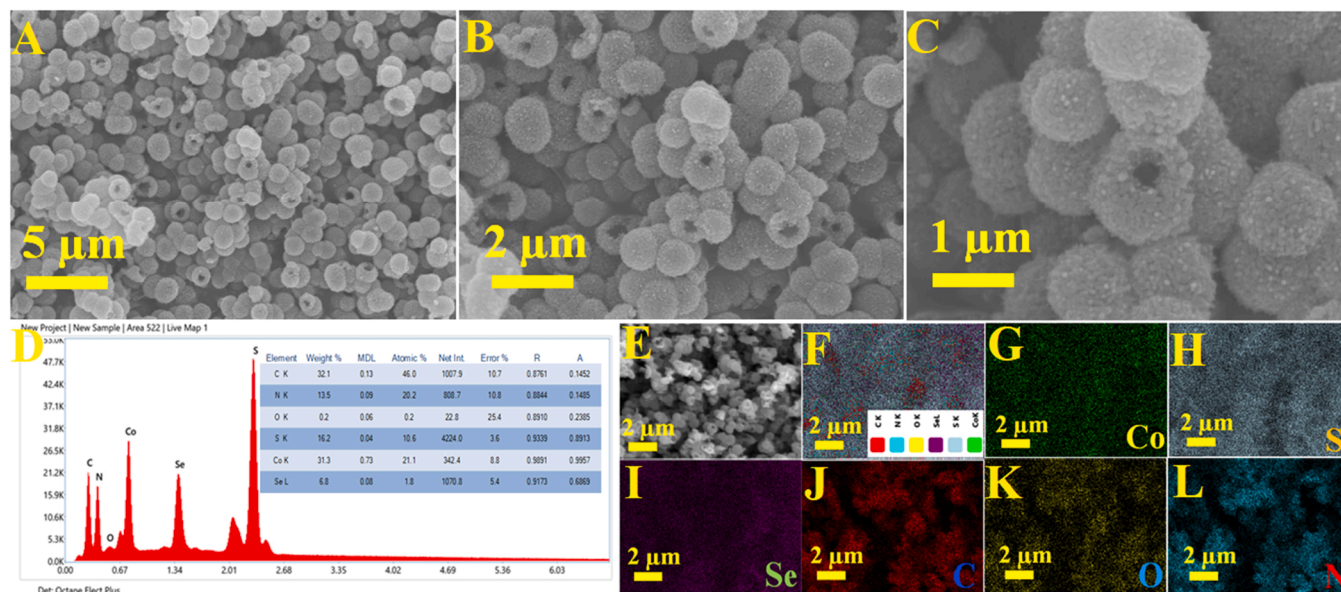
Fig. 2. (A-C) Different magnifications FESEM images of Se doped MOF CoS$_2$ hollow spheres, (D) EDX spectrum and inset image corresponding elemental composition, and (E-L) EDX mapping of Co, S, Se, C, N, and O of an individual Se doped MOF CoS$_2$ hollow spheres.
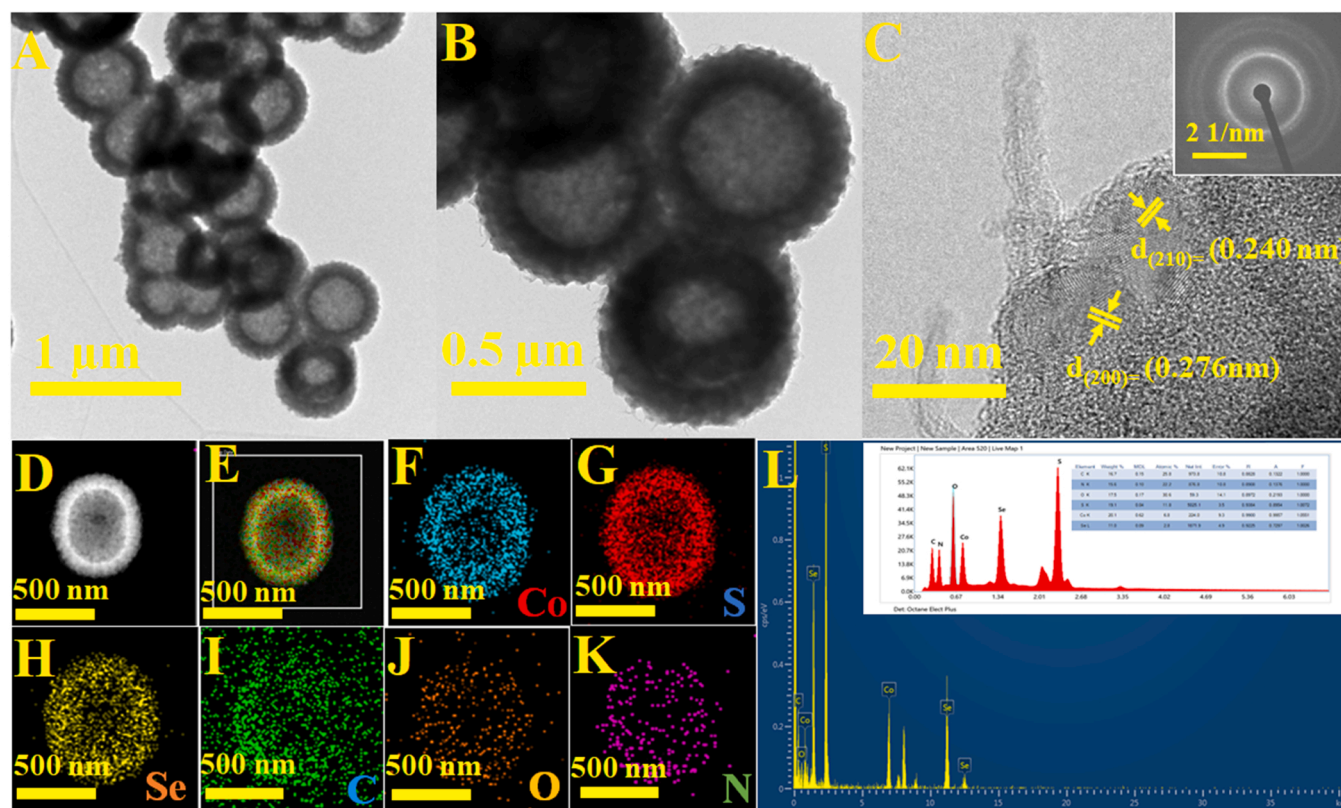

Fig. 3. (A-B) Different magnifications TEM images, (C) HRTEM image and inset image corresponding SAED patterns, (D-K) HR-EDX mapping, (L) HR-EDX spectrum and inset image corresponding elemental composition image of the Se doped MOF CoS$_2$ hollow spheres.

catalyst, with peaks at 27.2°, 32.3°, 36.3°, 55.1°, and 62.2° corresponding to the (111), (200), (210), (311), and (321) planes of CoS$_2$ (JCPDS 41–1471), respectively [48]. The XRD pattern of the MOF CoS$_2$ sample is given in Fig. 4B (b), which reveals similar diffraction peaks at 27.0°, 32.1°, 36.1°, 55.0°, and 62.0° matching to planes of (111), (200), (210), (311), and (321), which may be indexed standard CoS$_2$ pyrite structure (JCPDS 41–1471) [49], confirming complete conversion of

ZIF-67 into MOF CoS$_2$ hollow spheres. Under this condition, the peak value of the resultant product CoS$_2$ does not fluctuate much, indicating that the product's structure is not damaged. However, after doping Se, there is only a small shift in peaks with no Se-related new phases, indicating that the Se element was effectively doped into the Se-doped MOF CoS$_2$ hollow spheres structure. This behavior is most likely caused by the insertion of Se atoms, which increases interplanar distance
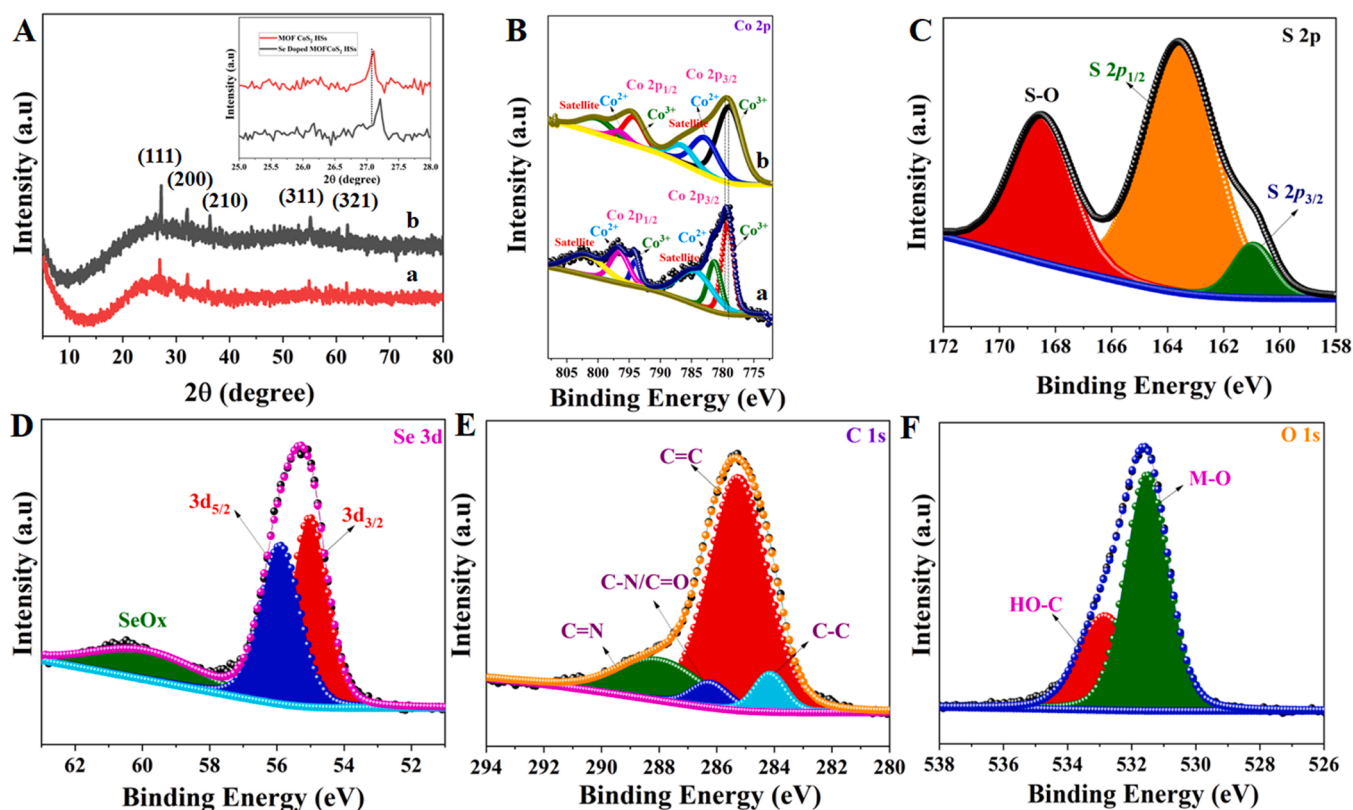
Fig. 4. (A) XRD patterns of (a) MOF CoS$_2$ hollow spheres and (b) Se-doped MOF CoS$_2$ hollow spheres. High-resolution XPS spectra of (B) Co 2p (a) and Co 2p (b), (C) S 2p, (D) Se 3d, (E) C 1 s, and (F) O 1 s in the Se-doped MOF CoS$_2$ hollow spheres (a), MOF CoS$_2$ hollow spheres (b) respectively.

due to Se's larger atomic radius than S [49]. Meanwhile, the positions of the distinct peaks are consistent with HRTEM findings. Fig. S4a shows MOF CoSe hollow spheres XRD peaks at 2θ = 30.6, 34.3, 36.2, 43.8, 47.9, 53.2, and 63.6°, correlating to the (101), (111), (200), (121), (211), (031), and (122) planes of CoSe (JCPDS card no. 00–053–0449) [50]. The XRD pattern of the as-synthesized ZIF-67 is shown in Fig. S4b and the diffraction peaks agree well with the existing literature [51]. To explore the chemical oxidation states, the typical elements in the Se-doped MOF CoS$_2$ hollow spheres are further studied using X-ray photoelectron spectroscopy (XPS). Fig. S5A shows the XPS survey spectra of possible elements including Co, S, Se, C, N, and O. Fig. 4B reveals two different peaks at 779.5 eV and 794.5 eV, which belong to Co 2p$_{3/2}$ and Co 2p$_{1/2}$, respectively. Notably, the binding energy of Co 2p$_{1/2}$ in the Se-doped MOF CoS$_2$ hollow spheres is positively shifted by roughly 0.3 eV when compared to CoS$_2$ [52]. The binding energy varies negatively by roughly 0.35 eV when compared to CoSe. In terms of Co 2p$_{3/2}$, the binding energy in Se-doped MOF CoS$_2$ hollow spheres is approximately 0.09 eV higher than in CoS$_2$, and approximately 0.33 eV lower than in CoSe. The findings show that the Se dopant can efficiently modify the electronic structure of Co, indicating the formation of new Co-Se bonds [53]. Additionally, the S 2p spectrum is in Fig. 4C shows two peaks corresponding to S 2p$_{3/2}$ (161.2 eV) and S 2p$_{1/2}$ (163.6 eV). The broad binding energy peak at 168.5 eV in the S 2p spectra might be the result of S partial oxidation after Se doping.[54] The binding energy peaks in Fig. 4D at 55.9 and 54.8 eV are ascribed to Se 3d$_{3/2}$ and Se 3d$_{5/2}$, respectively, and are comparable to previously reported Se-doped CoS$_2$ values [55]. Also, the broad peak at 59.9 eV correlates to the surface oxidation of the Se edges [54]. Aside from that, the C 1 s spectrum (Fig. 4E) reveals a mixture of the four distinct peaks of C-N bonds (287.8 eV), C-C bonds (284.1 eV), C=C bonds (285.2 eV), and carbon in C-O bonds (285.9 eV), showing the presence of residual oxygen-containing moieties [27]. The high-resolution O 1 s peaks can be found at binding energies of 531.5 eV for metal oxide (M-O or hydroxide

species), and 532.8 eV for C-OH, as depicted in Fig. 4F. Fig. S5B shows a high-resolution N 1 s spectrum indicating binding energies of 398.5 eV and 400.3 eV, which are pyridinic and graphitic nitrogen peaks [29]. The N$_2$ adsorption-desorption test was utilized to evaluate the sample's specific surface area and porous volumes. The existence of mesopores throughout the samples is demonstrated by the unique type IV adsorption isotherms for samples (Fig. SA6). The sample pore size variation is in Fig. S6B shows that the Se-doped MOF CoS$_2$ hollow sphere has some mesoporous range from 5 to 9 nm. Furthermore, the NPSCSs have a larger Brunauer-Emmett-Teller (BET) specific surface area of 198.89 m^{2}g^{-1}. The greater specific surface area of Se-doped MOF CoS$_2$ hollow spheres may be attributed to their distinctive hollow, porous, and mesoporous structure [50].

3.2. Electrochemical activity of Se-doped MOF CoS$_2$ hollow spheres towards OER

The electrochemical OER performance of Se-doped MOF CoS$_2$ hollow spheres was investigated in a 1.0 M KOH solution. In contrast, the OER performance of the MOF CoS$_2$ hollow spheres, MOF CoSe hollow spheres, MOF Co hollow spheres, bare CC, and IrO$_2$ were also assessed under identical experiment conditions, revealing that the greatest electrocatalytic activity is largely related to the development of Se doped MOF CoS$_2$ hollow spheres. Fig. 5A depicts the linear sweep voltammetric (LSV) profiles of the electrocatalysts evaluated in 1.0 M KOH solution at a sweep rate of 5 mV s^{-1}. In comparison to bare CC, which has basically no OER electrocatalytic activity, the OER performance of other catalysts is as follows: Se doped MOF CoS$_2$ hollow spheres > MOF CoS$_2$ hollow spheres > MOF CoSe hollow spheres> MOF Co hollow spheres. It is important to keep in mind that, as shown in Fig. 5A, Se doped MOF CoS$_2$ hollow spheres only provide a smaller overpotential of 290 mV to achieve a current density of 10 mA cm^2, which is only 20 mV higher than IrO$_2$ (270 mV) and less than MOF CoS$_2$ hollow spheres
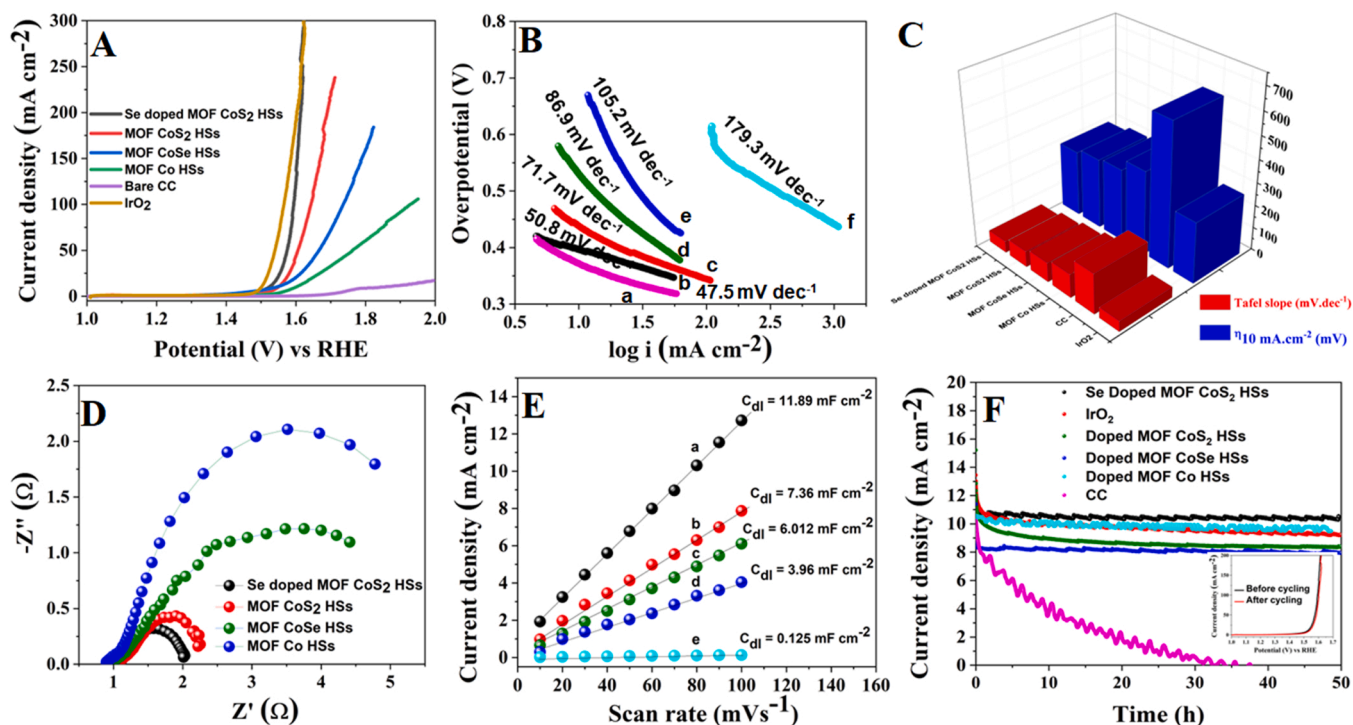
Fig. 5. (A) LSV curve of various OER electrocatalysts in a 1 M KOH solution at a scan rate of 5 mV s^{-1}, (B) Tafel plot of (a) IrO$_2$, (b) Se doped MOF CoS$_2$ hollow spheres, (c) MOF CoS$_2$ hollow spheres, (d) MOF CoSe hollow spheres, (e) MOF Co hollow spheres and (f) CC. (C) corresponding overpotential (η) vs Tafel slope values, (D) EIS spectra of various OER electrocatalysts, (E) C$_{dl}$ values of various electrocatalysts, (a) Se doped MOF CoS$_2$ hollow spheres, (b) MOF CoS$_2$ hollow spheres, (c) MOF CoSe hollow spheres, (d) MOF Co hollow spheres and (e) CC. (F) long-term stability test of various OER electrocatalysts and inset image LSV curves before and after 10,000 CV cycles of Se-doped MOF CoS$_2$ hollow spheres with 50 mVs^{-1} in 1.0 M KOH.

(310 mV) MOF CoSe hollow spheres (320 mV), MOF Co hollow spheres (370 mV) and bare CC (630 mV). A Tafel slope is another significant parameter of electrocatalysis efficiency. Se doped MOF CoS$_2$ hollow spheres displayed a low Tafel slope of 50.8 mV dec^{-1} in 1.0 M KOH solution (Fig. 5B), which was substantially lower than MOF CoS$_2$ hollow spheres (71.7 mV dec^{-1}), MOF CoSe hollow spheres (86.9 mV dec^{-1}), MOF Co hollow spheres (105.2 mV dec^{-1}) and bare CC (179.3 mV dec^{-1}), suggesting the fast OER kinetics mechanism. The overpotential (η) and Tafel slope (mV dec^{-1}) values (Fig. 3C) are dramatically lowered when the Se network is doped into the MOF CoS$_2$ hollow spheres because of increased water oxidation kinetics [53]. The electrochemical impedance spectroscopy (EIS) fitting findings revealed that the charge transfer resistance (R$_{ct}$) of Se-doped MOF CoS$_2$ hollow spheres (1.044 Ω) is lower than that of MOF CoS$_2$ hollow spheres (1.279 Ω), MOF CoSe hollow spheres (4.592 Ω), and MOF Co hollow spheres (8.625 Ω) (Fig. 5D). The findings indicate that the development of Se doped MOF CoS$_2$ hollow spheres and the doping of the strong (Se) metal-support interaction effect enhanced the electrical conductivity and interfacial charge transport capacity of the catalyst, boosted exposed active sites, and promoted electrocatalytic OER activity [25,26]. To determine the electrochemical surface area (ECSA) of the catalyst, CV performance within the double-layered (C$_{dl}$) region was performed on the as-prepared catalysts (Fig. S7). The C$_{dl}$ of Se doped MOF CoS$_2$ hollow spheres is 11.89 mF cm^{-2}, which is greater than the C$_{dl}$ of MOF CoS$_2$ hollow spheres (7.36 mF cm^{-2}), MOF CoSe hollow spheres (6.012 mF cm^{-2}), MOF Co hollow spheres (3.96 mF cm^{-2}), and bare CC (0.125 mF cm^{-2}) (Fig. 5E), implying that doping Se to MOF CoS$_2$ hollow spheres can increase the number of electrocatalytically active sites [24]. This occurs because the metallic Co-Se bond induces the formation of metal (oxy)hydroxide at the surface more easily than the Co-S bond, resulting in extremely efficient OER active sites and greatly increasing the ECSA during the OER process through the use of selenium leaching-induced surface reconstruction [26]. Remarkably, the synthesized Se-doped

MOF CoS$_2$ hollow spheres catalysts exhibit strong electrochemical stability. The polarization curves of the Se-doped MOF CoS$_2$ hollow spheres catalyst was nearly not altered after 10,000 cycles of scanning, as shown in the inset Fig. 5F. The current-time (i–t) experiment revealed that the current density was kept virtually consistent throughout 50 h. According to the findings, the Se-doped MOF CoS$_2$ hollow sphere catalyst exhibits outstanding long-term stability. The excellent OER activity of Se-doped MOF CoS$_2$ hollow spheres is equivalent to or better than that of recently published OER-based electrocatalysts (Table S1).

3.3. Electrochemical activity of Se-doped MOF CoS$_2$ hollow spheres towards ORR

To explore the ORR performances of Se-doped MOF CoS$_2$ hollow spheres, MOF CoS$_2$ hollow spheres, MOF CoSe hollow spheres, and MOF Co hollow spheres and bare GC, we carried out cyclic voltammogram (CV) measurements in a 0.1 M KOH solution with nitrogen and oxygen saturated solutions at a scan rate of 5 V s^{-1} (Fig. S8). The electro-catalytic ORR activities of the Se-doped MOF CoS$_2$ hollow spheres exhibit outstanding ORR catalytic activity. The electrocatalytic activities of ORR performance are also affected by the onset potential, peak potential, and peak current of the synthesized catalysts. Both the ORR onset potential and the peak potential are clearly shown to increase with an oxygen-saturated solution, implying that the ORR activities of the Se-doped MOF CoS$_2$ hollow spheres is superior. As demonstrated in Fig. 6A, the Se-doped MOF CoS$_2$ hollow spheres exhibit a unique ORR peak potential at 0.798 V vs RHE at a scanning rate of 5 V s^{-1}. The linear sweep voltammogram (LSV) of a Pt/C catalyst was studied for comparison (Fig. S9). The onset potential of the Pt/C catalyst is approximately 0.964 V vs RHE, whereas Se-doped MOF CoS$_2$ hollow spheres have a comparable onset potential (0.952 V). Furthermore, Se-doped MOF CoS$_2$ hollow spheres exhibit the greatest half-wave potential (E$_{1/2}$ = 0.88 V vs RHE) as well as the highest limiting current density (J$_L$) of
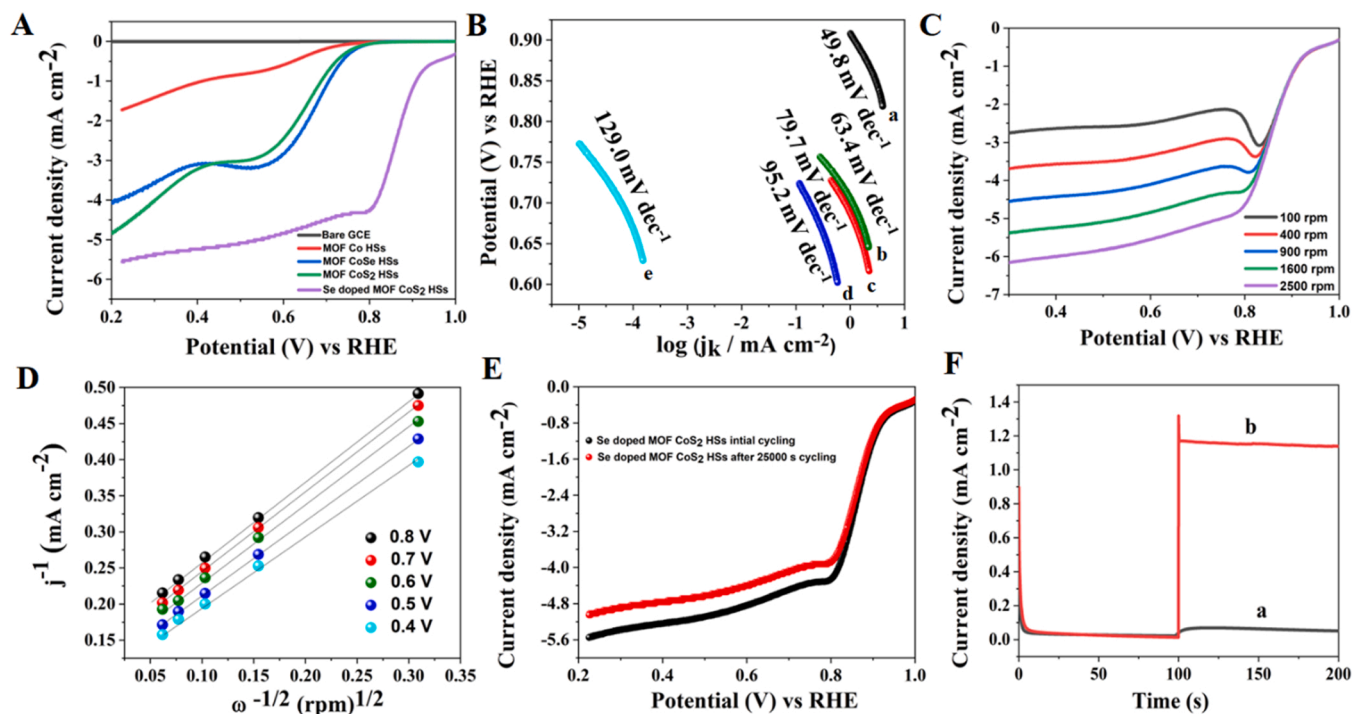
Fig. 6. ORR performances (A) LSV curve of various catalysts, (B) corresponding Tafel plot of (a) Se doped MOF CoS$_2$ hollow spheres, (b) MOF CoS$_2$ hollow spheres, (c) MOF CoSe hollow spheres, (d) MOF Co hollow spheres and (e) bare GC in 0.1 M KOH solutions, (C) LSV curves of Se doped MOF CoS$_2$ hollow spheres with a different rotating speed of RDE (100–2500 rpm), (D) K-L plots of Se doped MOF CoS$_2$ hollow spheres derived from LSV curves, (E) LSV curves of before and after cyclic stability studies, and (F) methanol tolerance test for (a) Se doped MOF CoS$_2$ hollow spheres and (b) Pt/C performed using chronoamperometry at a rotation speed of 1600 rpm in O$_2$ saturated 0.1 M KOH solution.

5.6 mA cm^{-2}, which is better than MOF CoS$_2$ hollow spheres (E$_{1/2}$ = 0.678 V vs RHE; J$_L$ = 4.03 mA cm^{-2}), MOF CoSe hollow spheres (E$_{1/2}$ = 0.647 V vs RHE; J$_L$ = 4.8 mA cm^{-2}), MOF Co hollow spheres (E$_{1/2}$ = 0.620 V vs RHE; J$_L$ = 1.7 mA cm^{-2}) and bare GC (E$_{1/2}$ = 0.58 V; J$_L$ = 0.008 mA cm^{-2}). Tafel slope can be used to further demonstrate a catalyst's inherent electrocatalytic activity. When compared to MOF CoS$_2$ hollow spheres (63.4 mV dec^{-1}) and MOF CoSe hollow spheres (79.7 mV dec^{-1}), MOF Co hollow spheres (95.2 mV dec^{-1}) and bare GC (129.03 mV dec^{-1}), the Se doped MOF CoS$_2$ hollow spheres had a lower Tafel slope of 49.8 mV dec^{-1} (Fig. 6B), indicating that the ORR on Se doped MOF CoS$_2$ hollow spheres occurred via a mechanism like the Pt/C catalyst. The rotating disk electrode (RDE) test was used to investigate the ORR process on the Se-doped MOF CoS$_2$ hollow spheres, MOF CoS$_2$ hollow spheres, MOF CoSe hollow spheres, and MOF Co hollow spheres. The polarization curves given in Fig. 6C showed that increasing the rotation rate increased the corresponding current density. The ORR kinetics of the Se-doped MOF CoS$_2$ hollow spheres catalyst was examined further using Koutecky–Levich plots of J^{-1} vs. ω$^{-1/2}$ derived from the LSV curves. As illustrated in Fig. 6D, the graphs exhibit excellent linearity at potentials of 0.4, 0.5, 0.6, 0.7, and 0.8 V. This occurrence not only implies first-order reaction kinetics in terms of dissolved O$_2$ concentration, but it also demonstrates that the number of electron transfers in the ORR was identical at various potentials and the Se doped MOF CoS$_2$ hollow spheres oxygen reduction followed a four-electron process based on the K–L equation data [50]. A cycling stability study was also conducted on the Se-doped MOF CoS$_2$ hollow sphere catalyst for 25,000 cycles. As illustrated in Fig. 6E, featureless LSV current profiles for Se doped MOF CoS$_2$ hollow spheres in an O$_2$-saturated electrolyte was observed, with no discernible change after 25,000 cycles. After cycles, Se-doped MOF CoS$_2$ hollow spheres showed a negative change in just 10 mV, revealing the increased stability of Se-doped MOF CoS$_2$ hollow spheres. Fuel cell technology is vital for many practical applications, and durability is essential. The chronoamperometric durability of Se-doped

MOF CoS$_2$ hollow spheres, MOF CoS$_2$ hollow spheres, MOF CoSe hollow spheres, and MOF Co hollow spheres and Pt/C at 0.65 V for 500000 s in an O$_2$-saturated 0.1 M KOH solution at 1600 rpm was also investigated (Fig. S10). The Se-doped MOF CoS$_2$ hollow spheres electrode retained more than 90% of its original current density after 500, 000 s of operating potential at 0.65 V vs RHE, but the other comparison materials including Pt/C electrode lost more than 30%, exhibiting the excellent stability of Se-doped MOF CoS$_2$ hollow spheres. In contrast to electrocatalytic activity, methanol tolerance is necessary to evaluate ORR performance in relevant applications. A current–time (i–t) test was also used to assess the electrocatalysts' methanol tolerance. Following the introduction of 0.5 M methanol into the electrolyte at 200 s, a notable increase in current with the Pt/C catalyst induced by the methanol oxidation process was detected, as depicted in Fig. 6F. On the contrary, Se-doped MOF CoS$_2$ hollow spheres was more consistent, with current retention of 98% after 200 s. This also demonstrates that the Se-doped MOF CoS$_2$ hollow spheres catalyst has higher methanol tolerance than the Pt/C catalyst. The foregoing findings indicate that Se-doped MOF CoS$_2$ hollow spheres have improved electrocatalytic activity, great methanol endurance, and excellent durability in the ORR, implying that it might be used as a replacement for benchmark catalysts-based catalysts in the ORR.

3.4. DFT and catalytic mechanism of Se-doped MOF CoS$_2$ hollow spheres

To explore the change in the structure and composition of the catalyst during the OER, we examined the XRD patterns, FESEM, HRTEM images, and energy-dispersive X-ray spectroscopy (EDS) data of the Se doped MOF CoS$_2$ hollow spheres sample before and after the OER test. The XRD patterns of after electrochemical stability, Se doped MOF CoS$_2$ hollow spheres decrease sharply in diffraction intensity and the peak widths expand when compared to the initial catalyst, as shown in Fig. S11. Furthermore, after the cyclic test, the crystal lattices are

unordered. These data support the hypothesis that the degree of metal oxyhydroxides in the Se-doped MOF CoS_2 hollow spheres increased during the OER, which is a key factor in its enhanced catalytic activity [7]. There is no structural degradation observed in FESEM, and the Se-doped MOF CoS_2 catalyst retains its hollow spherical morphology (Fig. S12). The EDX mapping reveals that Co, Se, S, O, C and N are still distributed uniformly inside the material (Fig. S12), and no additional species inclusion was observed after electrochemical cycles. Similarly, after the durability test, we employed TEM to assess the post-morphological characteristics of the Se-doped MOF CoS_2 hollow spheres catalyst. TEM images of the post-OER catalyst (Fig. S13) show no noticeable alterations in morphology, and the hollow spheres were more stable without degradation. Thus, the Se-doped MOF CoS_2 hollow spheres catalyst has excellent structural stability for OER activity. Take notice that in the XPS spectrum of the Se-doped MOF CoS_2 catalyst after the cyclic OER stability test, there are two new peaks generated at 780.3 eV and 788.3 eV corresponding to CoOOH and CoO, perhaps due to the sample being oxidized during the water oxidization process (Fig. S14A) [34]. Figure 14B displays high-resolution S 2p spectra for Se-doped MOF CoS_2 hollow spheres. Peaks at 166.3 eV are attributed to S-O species formed by surface oxidization. For S-Co species, the doublets between 163.5 and 161.7 eV can be ascribed to S $2p_{1/2}$ and S $2p_{3/2}$ [56]. After electrochemical stability of Se-doped MOF CoS_2 hollow spheres displays greater low-energy peaks for the S-Co species and weaker high-energy peaks for the S-O species, signifying a higher S-Co species density in electrochemical stability of Se-doped MOF CoS_2 hollow spheres. Thus, Co-S species are considered to promote the catalytic active site in these Se-doped CoS_2 [56]. The deconvoluted Se 3d XPS spectrum (Fig. S14C) demonstrates that the peak intensity of SeO_x increased following electrochemical testing due to the surface oxidation of Se under strongly alkaline conditions [22]. The high-resolution spectrum of O 1 s may be matched to four peaks at 529, 530.5, 531.2, and 532.6 eV, which correspond to the metal-oxygen (M-O), a hydroxyl group (OH), surface adsorbed oxygen and chemisorbed water molecules on the Se doped MOF CoS_2 catalyst, respectively (Fig. S14D) [50]. To

further understand the fundamental mechanism of Se-doped MOF CoS_2 hollow sphere high activity, we used DFT simulations to investigate the Gibbs free energy and density of state (DOS) variations during electrocatalysis. Fig. 7A and B show the crystal structure models of pure CoS_2 and Se-doped CoS_2. The insertion of Se leads certain S atoms to be replaced by Se. Fig. 7C, D exhibits density of states (DOS) plots. Since the distributions of CoS_2 and Se-doped CoS_2 are almost identical, Se-doping can preserve CoS_2's favorable electronic properties [57]. Following that, on CoS_2 and Se-doped CoS_2, three potential sites, the Co-site, the S-site, and the Se sites were explored. It is suggested that the outcomes of electrocatalyst OER are closely related to the atomic oxygen intermediate adsorption Gibbs free energy (ΔG_n *) on the electrocatalyst surface [56]. Using the optimized Se-doped CoS_2 model, we established a high correlation between the simulated and experimentally observed XRD patterns (JCPDS 41–1471). Considering the difference between the actual potential (maximum ΔG_n over the charge e) and the typical Nernstian potential (1.23 V vs. SHE), the change of the Gibbs free energies, ΔG_n ($\Delta G_n = 1, 4$), over the four essential OER phases was determined. As a result, the ΔG_n values of intermediates must be as close to each other as possible in order to minimize overpotential (η) [58]. Based on the revealed stable crystal face characterized by TEM and Se doing content determined by EDX, adsorbed oxygen intermediate on the (200) lattice face of CoS_2 and Se doped CoS_2 with Se doing content of 2% are constructed to investigate their ΔGn ($\Delta G_n = 1, 4$), as shown in Fig. 7E. The theoretical study revealed that Se-doped CoS_2 is a good OER electrocatalyst, with a theoretical overpotential (η) value of 0.54 V (Table S2). The formation of O* is the rate-determining step, and the binding energy of Co and O* is extremely weak. On the other hand, the CoS_2 has an overpotential (η) value of 0.88 V with the rate-determining step for the formation of the OOH* intermediate. This is due in large part to the significantly greater interaction between the surface Co atom and the O* intermediate [59]. The lowest theoretical overpotential values found Se doped CoS_2 that nearly matches the experimental data (Table S3). Furthermore, the ΔGn* at the Co sites of Se-doped CoS_2 (+0.44 eV) is substantially lower than that of pure CoS_2 (+0.85 eV),
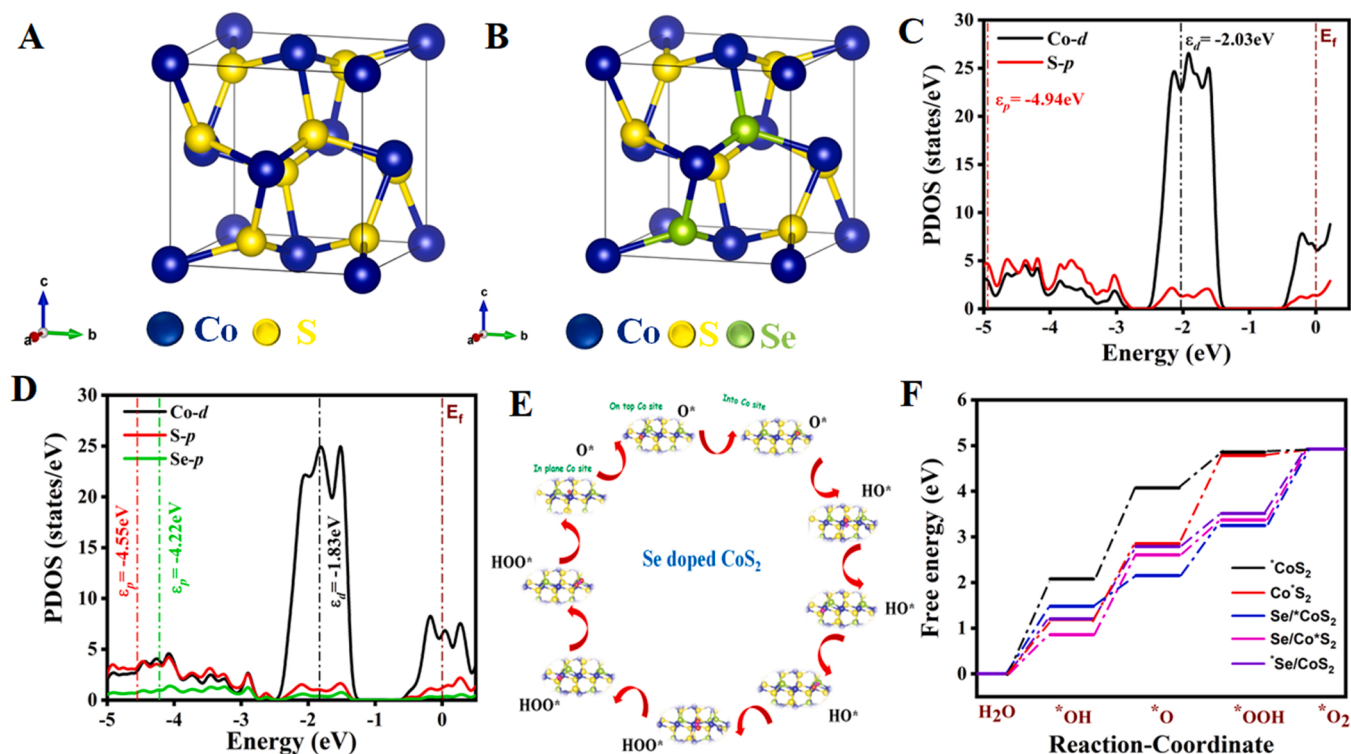

Fig. 7. Crystal structures of (A) CoS_2 and (B) Se-doped CoS_2 models, respectively. PDOS plots of (C) CoS_2 and (D) Se-doped CoS_2 models. (E) OER cycles for the cobalt terminal site of Se doped CoS_2 models. (F) Gibbs free energy of Se doped CoS_2 models (Co-sites and S-sites and Se sites).

implying that oxygen intermediate adsorption and desorption on Se-doped CoS_2 occurs at a much faster rate (Fig. 7F). The reduced ΔG_n * of the Co-site following Se doping suggests that the Se dopant can lower the OER energy barrier and enhance oxygen evolution (Table S4). As a result, our theoretical analyses show that only the interface of the Se-doped CoS_2 has improved OER activity. Both the ORR and OER processes are commonly recognized to need four elementary reaction steps, with the ORR pathway containing the formation of OOH* from adsorbed O_2, followed by a subsequent reduction to O* and OH* , and the OER process occurring in the opposite manner (complete equations are given in the ESI) [13]. Utilize the potential of a common plane in Fig. 3C by matching it to the CoS_2 (200) plane. This is made thermodynamically plausible by the similar distances between nearby atoms at each crystal plane. The Se-doped CoS_2 electrode offers amazing insight into the electron transfer pathways of exothermic reactions. Through careful analysis, it has been determined that all reaction steps occur spontaneously at a U value less than 0.51 V, suggesting that these reactions are highly favorable. The reaction steps $O_2(g)$ OOH* dominate the whole process (Fig. S15). At a potential of less than 0.51 V, the reaction step OH* + H^+ + e^- = $H_2O(l)$ + * was endothermic for the pure CoS_2. Theoretical simulations show that doping Se into CoS_2 can considerably increase ORR catalysis. This is because it could optimize the affinity of the catalyst surface with oxygen species, resulting in increased efficiency and performance.

3.5. Electrochemical activity of Se-doped MOF CoS_2 hollow spheres toward zinc-air batteries

To determine the feasibility of the as-synthesized Se doped MOF CoS_2 hollow spheres as a bifunctional catalyst, a homemade Zn-air battery was built using the Zn plate, the Se doped MOF CoS_2 hollow sphere loaded in carbon cloth, and 6.0 M KOH/0.2 M zinc acetate as the anode, air-cathode, and electrolyte, respectively. The open-circuit voltage (OCV) of the Se-doped MOF CoS_2 hollow sphere Zn-air battery is 1.459 V (Fig. 7A) which is higher than the benchmark catalyst (Pt/C/ IrO_2) (1.428 V). Furthermore, the Se-doped MOF CoS_2 hollow spheres ZnABs have a higher specific capacity of 620.67 mAh g_{Zn}^{-1} at a current density of 20 mA cm^{-2} than the Pt/C/IrO_2 based ZnABs (563.23 mAh g_{Zn}^{-1}) (Fig. 7B). In contrast to Pt/C, Fig. 7C illustrates the discharge and charge polarization curves for Zn-air batteries utilizing Se-doped MOF CoS_2 hollow spheres as the ORR and OER bifunctional catalyst. When particularly in comparison to a Zn-air battery with a Pt/C air-cathode, the Zn-air battery with the Se doped MOF CoS_2 hollow spheres air-cathode possesses a somewhat lower charge-discharge voltage range, showing strong rechargeability. The Zn-air battery constructed on the Se doped MOF CoS_2 hollow spheres air-cathode produced a discharge/ charge potential of 1.20 V/1.97 V with a lower voltage gap of 0.77 V and a high round-trip efficiency of 62%. The Se-doped MOF CoS_2 hollow spheres air-cathode displayed little power losses with a 0.13 V rise in the voltage gap after 500 cycles, however, Pt/C demonstrated a significantly higher spike in the voltage gap (0.38 V) under the same circumstances. The maximum power density of the Zn-air battery utilizing the Se doped MOF CoS_2 hollow spheres catalyst was measured to be 156.24 mW cm^{-2}, surpassing those of the Pt/C/IrO_2-based equivalent (104.56 mW cm^{-2}) (Fig. 7D). The galvanostatic discharge at 5 mA cm^{-2} was also used to assess the stability. The Se-doped MOF CoS_2 hollow spheres catalyst exhibits no discernible decline throughout the 100 h discharge, but the Pt/C + IrO_2 catalyst exhibits a noticeable diminution, confirming the much-increased endurance of the as-fabricated Se-doped MOF CoS_2 hollow spheres battery. The long-term durability of the zinc-air battery with the Se-doped MOF CoS_2 air cathode was tested using a galvanostatic charge-discharge technique for 5 min at 5 mA cm^{-2} charging and discharging (Fig. S16). Fig. 7 E, F schematic illustration of the constructed rechargeable liquid electrolyte-based zinc-air battery, as well as a digital image of liquid electrolytes with rechargeable zinc-air batteries based on the Se-doped MOF CoS_2 hollow spheres air cathode. The results showed that the zinc-air battery based on the Se-doped MOF CoS_2 hollow spheres air cathode possesses exceptional stability at 5 mA cm^{-2}, with the round-trip overpotential only marginally rising after 100 h. (Fig. 8).
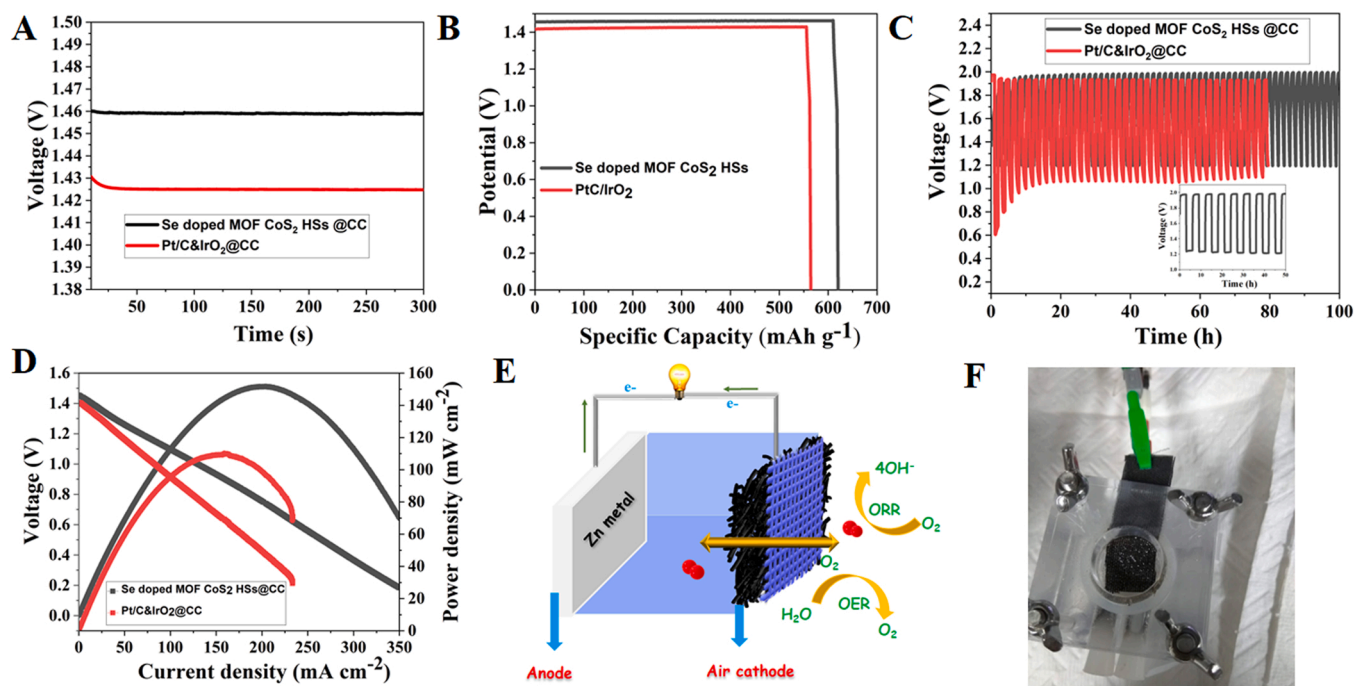

Fig. 8. Electrochemical performance of the fabricated rechargeable ZnABs. (A) Open-circuit potential plot. (B) The specific capacity of the Se-doped MOF CoS_2 hollow spheres and Pt/C + IrO_2 (1:1) based air cathode at 20 mA cm^{-2}. (C) Charge-discharge curves of Se-doped MOF CoS_2 hollow spheres and Pt/C + IrO_2 (1:1). (D) Discharge curve and corresponding power density curves of Se doped MOF CoS_2 hollow spheres and Pt/C + IrO_2 (1:1). (E) Schematic view illustrating the rechargeable ZnABs. (F) Photographic image of homemade ZnABs devices.

The Se-doped MOF CoS_2 hollow spheres catalyst exhibits high electrocatalytic activity for OER and ORR, as well as exceptional cycle stability and reversibility for ZnABs. The above-mentioned dominating OER, ORR, and ZnABs performance of Se-doped MOF CoS_2 hollow spheres may be explained as follows. First, the porous structure of Se-doped MOF CoS_2 hollow spheres may provide additional active catalytic sites and minimize electron transport routes throughout the electrochemical process. Additionally, the hollow design may reduce inner stress during cycling, thereby extending cycling life. Second, the Se-doped and conductive in situ-grown N-doped graphitic carbon matrix may effectively reduce internal resistance while offering perfect, uninterrupted electronic transmission channels. Finally, the well-coupled interface between Se and MOF CoS_2/NC completely leverages the inherent properties of each Se and CoS_2/NC, resulting in more active sites between the two phases and robust electron transport. The outstanding OER, ORR, and ZnABs performance of Se-doped MOF CoS_2 hollow spheres reveals electrocatalysis and energy storage applications.

4. Conclusions

In summary, a simple vapor sulfuration and selenization treatment technique were employed to synthesize Se-doped MOF CoS_2 hollow spheres. The strategic combination of methanol as a solvent and SO_4^{-2} as a ligand increased the nucleation rate and significant subassembly of Co^{2+} and 2-MIM ions, allowing the template-free synthesis of basic spherical hollows during solution mixing. The resulting Se-doped MOF CoS_2 hollow spheres have a significant active surface area, exposing numerous active sites, and the material's electronic structure may have changed after doping with Se, promoting the entire electrochemical reaction, which exhibits high bifunctional ORR/OER electrocatalytic activity and stability. Moreover, DFT simulation results show that Se doping can optimize ΔGn^* on Co sites, boosting the intrinsic OER activity of Se-doped CoS_2. Because of its bifunctionality, the as-fabricated Zn-air battery device (Se doped MOF CoS_2 hollow spheres /Zn foil) has an appealing operating performance with a high discharge voltage of 1.20 V and a low charge voltage of 1.97 V (@ 5 mA cm^{-2}), exceeding the majority of previously published MOF based catalysts. The Zn-air battery based on Se-doped MOF CoS_2 hollow spheres is expected to be beneficial in extremely dependable and efficient systems for energy storage. This low-cost synthesis process may open the route for the development of additional novel hybrid materials that can act as efficient catalysts in applications involving renewable energies.

CRediT authorship contribution statement

Alagan Muthurasu: Conceptualization, Methodology, Investigation, Writing – review & editing, Writing – original draft. **Prabhakaran Sampath**: DFT calculation for ORR and OER. **Tae Hoon Ko**: Visualization. **Prakash Chandra Lohani**: Visualization. **Ishwor Pathak**: Visualization**. Debendra Acharya**: Visualization. **Kisan Chhetri**: Visualization. **Do Hwan Kim.** DFT calculation for ORR and OER. **Hak Yong Kim**: Supervision, Writing – review & editing, Writing – original draft.

Declaration of Competing Interest

The authors declare that they have no known competing for financial interests or personal relationships that could have appeared to influence the work reported in this paper.

Data Availability

Data will be made available on request.

Appendix A. Supporting information

Supplementary data associated with this article can be found in the online version at doi:10.1016/j.apcatb.2023.122523.

References

[1] J. Luo, S. Zhang, M. Sun, L. Yang, S. Luo, J.C. Crittenden, A critical review on energy conversion and environmental remediation of photocatalysts with remodeling crystal lattice, surface, and interface, ACS Nano 13 (2019) 9811–9840, https://doi.org/10.1021/acsnano.9b03649.

[2] C. Zhu, H. Wang, C. Guan, Recent progress on hollow array architectures and their applications in electrochemical energy storage, Nanoscale Horiz. 5 (2020) 1188–1199, https://doi.org/10.1039/d0nh00332h.

[3] S. Lee, J. Choi, M. Kim, J. Park, M. Park, J. Cho, Material design and surface chemistry for advanced rechargeable zinc-air batteries, Chem. Sci. 13 (2022) 6159–6180, https://doi.org/10.1039/d1sc07212a.

[4] X. Zheng, N. Mohammadi, A. Moreno Zuria, M. Mohamedi, Advanced zinc-air batteries with free-standing hierarchical nanostructures of the air cathode for portable applications, ACS Appl. Mater. Interfaces 13 (2021) 61374–61385, https://doi.org/10.1021/acsami.1c22371.

[5] X. Yu, T. Zhou, J. Ge, C. Wu, Recent advances on the modulation of electrocatalysts based on transition metal nitrides for the rechargeable Zn-Air battery, ACS Mater. Lett. 2 (2020) 1423–1434, https://doi.org/10.1021/acsmaterialslett.0c00339.

[6] A.K. Worku, D.W. Ayele, N.G. Habtu, Recent advances and future perspectives in the engineering of bifunctional electrocatalysts for rechargeable zinc–air batteries, Mater. Today Adv. 9 (2021), 100116, https://doi.org/10.1016/j.mtadv.2020.100116.

[7] C. Zhou, X. Chen, S. Liu, Y. Han, H. Meng, Q. Jiang, S. Zhao, F. Wei, J. Sun, T. Tan, R. Zhang, Superdurable bifunctional oxygen electrocatalyst for high-performance zinc-air batteries, J. Am. Chem. Soc. 144 (2022) 2694–2704, https://doi.org/10.1021/jacs.1c11675.

[8] M. Xiong, D.G. Ivey, Sequentially electrodeposited MnO$_X$ /Co-Fe as bifunctional electrocatalysts for rechargeable zinc-air batteries, J. Electrochem. Soc. 164 (2017) A1012–A1021, https://doi.org/10.1149/2.0481706jes.

[9] A. Loh, D.P. Trudgeon, X. Li, M.C. Liu, L. Bin Kong, F.C. Walsh, Selection of oxygen reduction catalysts for secondary tri-electrodezinc–air batteries, Sci. Rep. 12 (2022) 1–16, https://doi.org/10.1038/s41598-022-10671-5.

[10] S. Askari, D. Mariotti, R. McGlynn, J. Benedikt, Air-Cathode with 3D multiphase electrocatalyst interface design for high-efficiency and durable rechargeable zinc–air batteries, Energy Technol. 9 (2021) 1–10, https://doi.org/10.1002/ente.202000999.

[11] L. Bai, Z. Duan, X. Wen, J. Guan, Bifunctional atomic iron-based catalyst for oxygen electrode reactions, J. Catal. 378 (2019) 353–362, https://doi.org/10.1016/j.jcat.2019.09.009.

[12] Z. Zeng, G. Fu, H. Bin Yang, Y. Yan, J. Chen, Z. Yu, J. Gao, L.Y. Gan, B. Liu, P. Chen, Bifunctional N-CoSe$_2$/3D-MXene as highly efficient and durable cathode for rechargeable Zn-Air battery, ACS Mater. Lett. 1 (2019) 432–439, https://doi.org/10.1021/acsmaterialslett.9b00337.

[13] M. Mechili, C. Vaitsis, N. Argirusis, P.K. Pandis, G. Sourkouni, C. Argirusis, Research progress in transition metal oxide based bifunctional electrocatalysts for aqueous electrically rechargeable zinc-air batteries, Renew. Sustain. Energy Rev. 156 (2022), 111970, https://doi.org/10.1016/j.rser.2021.111970.

[14] J. Yin, J. Jin, H. Lin, Z. Yin, J. Li, M. Lu, L. Guo, P. Xi, Y. Tang, C.H. Yan, Optimized metal chalcogenides for boosting water splitting, Adv. Sci. 7 (2020), https://doi.org/10.1002/advs.201903070.

[15] J. Huang, Y. Jiang, T. An, M. Cao, Increasing the active sites and intrinsic activity of transition metal chalcogenide electrocatalysts for enhanced water splitting, J. Mater. Chem. A 8 (2020) 25465–25498, https://doi.org/10.1039/d0ta08802a.

[16] Y. Hou, M. Qiu, G. Nam, M.G. Kim, T. Zhang, K. Liu, X. Zhuang, J. Cho, C. Yuan, X. Feng, Integrated hierarchical cobalt sulfide/Nickel selenide hybrid nanosheets as an efficient three-dimensional electrode for electrochemical and photoelectrochemical water splitting, Nano Lett. 17 (2017) 4202–4209, https://doi.org/10.1021/acs.nanolett.7b01030.

[17] S. Wan, W. Jin, X. Guo, J. Mao, L. Zheng, J. Zhao, J. Zhang, H. Liu, C. Tang, Self-templating construction of porous CoSe$_2$ nanosheet arrays as efficient bifunctional electrocatalysts for overall water splitting, ACS Sustain. Chem. Eng. 6 (2018) 15374–15382, https://doi.org/10.1021/acssuschemeng.8b03804.

[18] Y. Chen, S. Xu, S. Zhu, R.J. Jacob, G. Pastel, Y. Wang, Y. Li, J. Dai, F. Chen, H. Xie, B. Liu, Y. Yao, L.G. Salamanca-Riba, M.R. Zachariah, T. Li, L. Hu, Millisecond synthesis of CoS nanoparticles for highly efficient overall water splitting, Nano Res. 12 (2019) 2259–2267, https://doi.org/10.1007/s12274-019-2304-0.

[19] S. Hyun, S. Shanmugam, Hierarchical nickel-cobalt dichalcogenide nanostructure as an efficient electrocatalyst for oxygen evolution reaction and a Zn-Air battery, ACS Omega 3 (2018) 8621–8630, https://doi.org/10.1021/acsomega.8b01375.

[20] L. Lei, D. Huang, C. Zhang, R. Deng, S. Chen, Z. Li, F dopants triggered active sites in bifunctional cobalt sulfide@nickel foam toward electrocatalytic overall water splitting in neutral and alkaline media: Experiments and theoretical calculations, J. Catal. 385 (2020) 129–139, https://doi.org/10.1016/j.jcat.2020.03.012.

[21] Y. Li, Z. Mao, Q. Wang, D. Li, R. Wang, B. He, Y. Gong, H. Wang, Hollow nanosheet array of phosphorus-anion-decorated cobalt disulfide as an efficient electrocatalyst for overall water splitting, Chem. Eng. J. 390 (2020), 124556, https://doi.org/10.1016/j.cej.2020.124556.

[22] Q. Dong, Q. Wang, Z. Dai, H. Qiu, X. Dong, MOF-Derived Zn-Doped CoSe₂ as an efficient and stable free-standing catalyst for oxygen evolution reaction, ACS Appl. Mater. Interfaces 8 (2016) 26902–26907, https://doi.org/10.1021/acsami.6b10160.

[23] S. Kumar, M.B. Gawande, J. Kopp, S. Kment, R.S. Varma, R. Zbořil, P- and F-co-doped carbon nitride nanocatalysts for photocatalytic co2 reduction and thermocatalytic furanics synthesis from sugars, ChemSusChem 13 (2020) 5231–5238, https://doi.org/10.1002/cssc.202001172.

[24] Y. Song, X. Zhao, Z.H. Liu, Surface selenium doped hollow heterostructure/defects Co-Fe sulfide nanoboxes for enhancing oxygen evolution reaction and supercapacitors, Electrochim. Acta 374 (2021), 137962, https://doi.org/10.1016/j.electacta.2021.137962.

[25] Q. Wang, Y. Huang, L. Huang, Y. Wu, S. Ren, Se doping regulates the activity of NiTe₂ for electrocatalytic hydrogen evolution reaction, J. Phys. Chem. C. 124 (2020) 26793–26800, https://doi.org/10.1021/acs.jpcc.0c08080.

[26] W. Deng, W. Xie, D. Li, Y. Gai, Z. Chen, J. Yu, R. Yang, X. Bao, F. Jiang, Controllable tuning of polymetallic Co-Ni-Ru-S-Se ultrathin nanosheets to boost electrocatalytic oxygen evolution, NPG Asia Mater. 14 (2022), https://doi.org/10.1038/s41427-022-00373-9.

[27] A. Muthurasu, K. Chhetri, B. Dahal, H.Y. Kim, Ruthenium nanoparticles integrated bimetallic metal-organic framework electrocatalysts for multifunctional electrode materials and practical water electrolysis in seawater, Nanoscale (2022) 6557–6569, https://doi.org/10.1039/d2nr04664h.

[28] Y. Xie, J. Cao, X. Wang, W. Li, L. Deng, S. Ma, H. Zhang, C. Guan, W. Huang, MOF-Derived Bifunctional Co₀.₈₅Se nanoparticles embedded in N-Doped carbon nanosheet arrays as efficient sulfur hosts for lithium-sulfur batteries, Nano Lett. 21 (2021) 8579–8586, https://doi.org/10.1021/acs.nanolett.1c02037.

[29] A. Muthurasu, G.P. Ojha, M. Lee, H.Y. Kim, Zeolitic imidazolate framework derived Co₃S₄ hybridized MoS₂–Ni₃S₂ heterointerface for electrochemical overall water splitting reactions, Electrochim. Acta 334 (2020), 135537, https://doi.org/10.1016/j.electacta.2019.135537.

[30] C. Liang, X. Zhang, P. Feng, H. Chai, Y. Huang, ZIF-67 derived hollow cobalt sulfide as superior adsorbent for effective adsorption removal of ciprofloxacin antibiotics, Chem. Eng. J. 344 (2018) 95–104, https://doi.org/10.1016/j.cej.2018.03.064.

[31] B. Zhang, G. Yang, C. Li, K. Huang, J. Wu, S. Hao, J. Feng, D. Peng, Y. Huang, Phase controllable fabrication of zinc cobalt sulfide hollow polyhedra as high-performance electrocatalysts for the hydrogen evolution reaction, Nanoscale 10 (2018) 1774–1778, https://doi.org/10.1039/c7nr08097b.

[32] X. Song, X. Jiang, F. Cheng, J. Earnshaw, J. Na, X. Li, Y. Yamauchi, Hollow carbon-based nanoarchitectures based on ZIF: inward/outward contraction mechanism and beyond, Small 17 (2021), https://doi.org/10.1002/smll.202004142.

[33] P. Zeng, J. Li, M. Ye, K. Zhuo, Z. Fang, In situ formation of Co₉S₈/N-C hollow nanospheres by pyrolysis and sulfurization of ZIF-67 for high-performance lithium-ion battry, Chem. - A Eur. J. 23 (2017) 9517–9524, https://doi.org/10.1002/chem.201700881.

[34] T. Mukhiya, A. Muthurasu, A.P. Tiwari, K. Chhetri, S.H. Chae, H. Kim, B. Dahal, B. M. Lee, H.Y. Kim, Integrating the essence of a metal-organic framework with electrospinning: a new approach for making a metal nanoparticle confined N-Doped carbon nanotubes/porous carbon nanofibrous membrane for energy storage and conversion, ACS Appl. Mater. Interfaces 13 (2021) 23732–23742, https://doi.org/10.1021/acsami.1c04104.

[35] C. Zhu, Y. Ma, W. Zang, C. Guan, X. Liu, S.J. Pennycook, J. Wang, W. Huang, Conformal dispersed cobalt nanoparticles in hollow carbon nanotube arrays for flexible Zn-air and Al-air batteries, Chem. Eng. J. 369 (2019) 988–995, https://doi.org/10.1016/j.cej.2019.03.147.

[36] A.S. Botana, M.R. Norman, Electronic structure and magnetism of transition metal dihalides: Bulk to monolayer, Phys. Rev. Mater. 3 (2019) 1–7, https://doi.org/10.1103/PhysRevMaterials.3.044001.

[37] G. Kresse, J. Hafner, Norm-conserving and ultrasoft pseudopotentials for first-row and transition elements, J. Phys. Condens. Matter 6 (1994) 8245–8257, https://doi.org/10.1088/0953-8984/6/40/015.

[38] S. Ehrlich, J. Moellmann, W. Reckien, T. Bredow, S. Grimme, System-dependent dispersion coefficients for the DFT-D3 treatment of adsorption processes on ionic surfaces, ChemPhysChem 12 (2011) 3414–3420, https://doi.org/10.1002/cphc.201100521.

[39] O.J. and O.K.A. Peter E. Blochl, 1994. Improved tetrahedron, Phys. Rev. 8. 49 (1994) 16223.

[40] S. Park, S. Kim, H.J. Kim, C.W. Lee, H.J. Song, S.W. Seo, H.K. Park, D.W. Kim, K. S. Hong, Hierarchical assembly of TiO₂.SrTiO₃ heterostructures on conductive SnO₂ backbone nanobelts for enhanced photoelectrochemical and photocatalytic performance, J. Hazard. Mater. 275 (2014) 10–18, https://doi.org/10.1016/j.jhazmat.2014.04.019.

[41] D.K. Lee, I.S. Cho, D.K. Yim, J.H. Noh, K.S. Hong, D.W. Kim, Synthesis and photoactivity of hetero-nanostructured SrTiO₃, J. Ceram. Soc. Jpn. 118 (2010) 876–880, https://doi.org/10.2109/jcersj2.118.876.

[42] S. Park, S. Lee, S.W. Seo, S.D. Seo, C.W. Lee, D. Kim, D.W. Kim, K.S. Hong, Tailoring nanobranches in three-dimensional hierarchical rutile heterostructures: a case study of TiO₂-SnO₂, CrystEngComm 15 (2013) 2939–2948, https://doi.org/10.1039/c3ce26722a.

[43] C. Chen, A. Wu, H. Yan, Y. Xiao, C. Tian, H. Fu, Trapping [PMo₁₂O₄₀]³⁻ clusters into pre-synthesized ZIF-67 toward Mo: XCoxC particles confined in uniform carbon polyhedrons for efficient overall water splitting, Chem. Sci. 9 (2018) 4746–4755, https://doi.org/10.1039/c8sc01454j.

[44] W. Weng, J. Lin, Y. Du, X. Ge, X. Zhou, J. Bao, Template-free synthesis of metal oxide hollow micro-/nanospheres: Via Ostwald ripening for lithium-ion batteries, J. Mater. Chem. A 6 (2018) 10168–10175, https://doi.org/10.1039/c8ta03161d.

[45] B. Mortazavi, A. Rajabpour, S. Ahzi, Y. Rmond, S. Mehdi Vaez Allaei, Nitrogen doping and curvature effects on thermal conductivity of graphene: a non-equilibrium molecular dynamics study, Solid State Commun. 152 (2012) 261–264, https://doi.org/10.1016/j.ssc.2011.11.035.

[46] Z.T. Shi, Y. Qi, J. Zhang, C.C. Guo, Z.H. Zhu, Carbon-Based metallic cobalt pyrite nanotubes as stable electrode materials for electrochemical hydrogen evolution, ACS Appl. Nano Mater. 3 (2020) 8335–8342, https://doi.org/10.1021/acsanm.0c01746.

[47] J. Yin, Y. Li, F. Lv, M. Lu, K. Sun, W. Wang, L. Wang, F. Cheng, Y. Li, P. Xi, S. Guo, Oxygen vacancies dominated NiS₂/CoS₂ interface porous nanowires for portable Zn–Air batteries driven water splitting devices, Adv. Mater. 29 (2017) 1–8, https://doi.org/10.1002/adma.201704681.

[48] M.S. Faber, R. Dziedzic, M.A. Lukowski, N.S. Kaiser, Q. Ding, S. Jin, High-performance electrocatalysis using metallic cobalt pyrite (CoS₂) micro- and nanostructures, J. Am. Chem. Soc. 136 (2014) 10053–10061, https://doi.org/10.1021/ja5054099w.

[49] Z. Li, Z. Jiang, W. Zhu, C. He, P. Wang, X. Wang, T. Li, L. Tian, Facile preparation of CoSe₂ nano-vesicle derived from ZIF-67 and their application for efficient water oxidation, Appl. Surf. Sci. 504 (2020), 144368, https://doi.org/10.1016/j.apsusc.2019.144368.

[50] A. Muthurasu, B. Dahal, T. Mukhiya, K. Chhetri, H.Y. Kim, Fabrication of nonmetal-modulated dual metal-organic platform for overall water splitting and rechargeable Zinc-Air batteries, ACS Appl. Mater. Interfaces 12 (2020) 41704–41717, https://doi.org/10.1021/acsami.0c09794.

[51] A. Muthurasu, S.H. Chae, T. Hoon Ko, P. Chandra Lohani, H. Yong Kim, Highly ordered nanoarrays catalysts embedded in carbon nanotubes as highly efficient and robust air electrode for flexible solid-state rechargeable zinc-air batteries, J. Colloid Interface Sci. 616 (2022) 679–690, https://doi.org/10.1016/j.jcis.2022.02.097.

[52] J. Zhang, Y. Liu, C. Sun, P. Xi, S. Peng, D. Gao, D. Xue, Accelerated hydrogen evolution reaction in CoS₂ by transition-metal doping, ACS Energy Lett. 3 (2018) 779–786, https://doi.org/10.1021/acsenergylett.8b00066.

[53] Y. Gui, X. Liu, Y. Dou, L. Zhang, M. Al-Mamun, L. Jiang, H. Yin, C.T. He, H. Zhao, Manipulating the assembled structure of atomically thin CoSe₂ nanomaterials for enhanced water oxidation catalysis, Nano Energy 57 (2019) 371–378, https://doi.org/10.1016/j.nanoen.2018.12.063.

[54] X. Han, X. Wu, Y. Deng, J. Liu, J. Lu, C. Zhong, W. Hu, Ultrafine Pt nanoparticle-decorated pyrite-type CoS₂ nanosheet arrays coated on carbon cloth as a bifunctional electrode for overall water splitting, Adv. Energy Mater. 8 (2018), https://doi.org/10.1002/aenm.201800935.

[55] K. Li, J. Zhang, R. Wu, Y. Yu, B. Zhang, Anchoring CoO domains on CoSe₂ nanobelts as bifunctional electrocatalysts for overall water splitting in neutral media, Adv. Sci. 3 (2015) 11500426, https://doi.org/10.1002/advs.201500426.

[56] G. Qu, T. Wu, Y. Yu, Z. Wang, Y. Zhou, Z. Tang, Q. Yue, Rational design of phosphorus-doped cobalt sulfides electrocatalysts for hydrogen evolution, Nano Res. 12 (2019) 2960–2965, https://doi.org/10.1007/s12274-019-2538-x.

[57] B. Kim, I. Park, G. Yoon, J.S. Kim, H. Kim, K. Kang, Atomistic investigation of doping effects on electrocatalytic properties of cobalt oxides for water oxidation, Adv. Sci. 5 (2018), https://doi.org/10.1002/advs.201801062.

[58] H. Li, W. Yuan, Q. Wang, X. Cui, J. Jiang, S. Chen, L. Song, X. Guo, Two-dimensional cobalt oxy-hydrate sulfide nanosheets with modified t₂g Orbital State of CoO₆₋ₓ octahedron for efficient overall water splitting, ACS Sustain. Chem. Eng. 7 (2019) 17325–17334, https://doi.org/10.1021/acssuschemeng.9b04256.

[59] B.H.R. Suryanto, Y. Wang, R.K. Hocking, W. Adamson, C. Zhao, Overall electrochemical splitting of water at the heterogeneous interface of nickel and iron oxide, Nat. Commun. 10 (2019) 5599, https://doi.org/10.1038/s41467-019-13415-8.